Common Origin of the Circular-Dichroism Pattern in Angle-Resolved Photoemission Spectroscopy of $SrTiO_3$ and $Cu_xBi_2Se_3$

Y. Ishida,[1] H. Kanto,[1] A. Kikkawa,[2] Y. Taguchi,[2,3] Y. Ito,[1] Y. Ota,[1] K. Okazaki,[1] W. Malaeb,[1] M. Mulazzi,[1,*] M. Okawa,[1] S. Watanabe,[1] C.-T. Chen,[4] M. Kim,[5] C. Bell,[5,6] Y. Kozuka,[5] H. Y. Hwang,[2,5,6] Y. Tokura,[2,3,7] and S. Shin[1,8]

[1]*ISSP, University of Tokyo, Kashiwa, Chiba 277-8581, Japan*
[2]*Correlated Electron Research Group (CERG), RIKEN Advanced Science Institute, Wako 351-0198, Japan*
[3]*Cross-Correlated Materials Research Group (CMRG), RIKEN Advanced Science Institute, Wako 351-0198, Japan*
[4]*Technical Institute of Physics and Chemistry, Chinese Academy of Science, Zhongguancun, Beijing 100080, China*
[5]*Department of Advanced Materials Science, University of Tokyo, Kashiwa, Chiba 277-8561, Japan*
[6]*Department of Applied Physics and Stanford Institute for Materials and Energy Science, Stanford University, Stanford, California 94305, USA*
[7]*Department of Applied Physics, University of Tokyo, Tokyo 113-8656, Japan*
[8]*CREST, Japan Science and Technology Agency, Tokyo 102-0075, Japan*

(Received 2 May 2011; revised manuscript received 30 June 2011; published 9 August 2011)

Circular dichroism in the angular distribution of photoelectrons from $SrTiO_3$:Nb and $Cu_xBi_2Se_3$ is investigated by 7-eV laser angle-resolved photoemission spectroscopy. In addition to the well-known node that occurs in the circular dichroism pattern when the incidence plane matches the mirror plane of the crystal, we show that another type of node occurs when the mirror plane of the crystal is vertical to the incidence plane and the electronic state is two-dimensional. The flower-shaped circular dichroism patterns in the angular distribution occurring around the Fermi level of $SrTiO_3$:Nb and around the Dirac point of $Cu_xBi_2Se_3$ are explained on equal footings. We point out that the penetration depth of the topological states of $Cu_xBi_2Se_3$ depends on momentum.

DOI: 10.1103/PhysRevLett.107.077601 PACS numbers: 79.60.−i, 73.20.At

The interaction of light with matter depends on the polarization of the photons. Circular dichroism (CD) is a phenomenon in which the response of a system to left and right circularly polarized light is different. CD can be microscopically attributed to the difference in the material's response against opposite helicities of the photons. Thus, CD has been actively used for studying magnetic materials or those having strong spin-orbit interactions [1–3]. Alternatively, left and right circular polarizations are exchanged by a mirror operation, and therefore CD is active when the measurement breaks symmetry with respect to the reflection; i.e., CD occurs when the experimental geometry has "handedness" [4,5].

In angle-resolved photoemission spectroscopy (ARPES), light is shined on a crystal and the energy-and-angle distribution of the photoelectrons is recorded. The band structures of crystals and crystal surfaces are traced by ARPES, and the information is further enriched by investigating the CD in the angular distribution (CDAD) of the photoelectrons [3–12]. For example, a node in CDAD occurs when the incidence plane and the mirror plane of the crystal are matched [5]. This vertical node, which occurs due to reasons of symmetry, has been utilized in various ARPES studies [7–12]. In this Letter, we show that there is another type of node, a *horizontal* node, which occurs due to a combination of the symmetry and dimensionality of the initial electronic state. We first investigate photoemission matrix elements and derive the condition for the occurrence of the horizontal node. Then we introduce and derive information from the horizontal nodes occurring in the CDADs of $SrTiO_3$:Nb and $Cu_xBi_2Se_3$.

The experimental geometry of 7-eV laser ARPES [13] is shown in Fig. 1(a). By using an orthogonal basis fixed on the sample (we take $\boldsymbol{e}_x$ along the sample rotation axis and $\boldsymbol{e}_y$ along the sample surface), the vector potentials for right ($\boldsymbol{A}^+$) and left ($\boldsymbol{A}^-$) circular polarizations are described as $\boldsymbol{A}^{\pm} = \boldsymbol{A}^{\pm}_{\mathrm{pes}} e^{-i(\omega t+\varphi)} + \mathrm{c.c.}$, where $\boldsymbol{A}^{\pm}_{\mathrm{pes}} = \frac{A}{2}(-1, \mp i\cos\eta, \mp i\sin\eta)$, η is the angle between the laser beam and $\boldsymbol{e}_z$, and φ is a phase. The analyzer collects photoelectrons emitted within the acceptance angle $|\alpha| < 18°$ ($\alpha = 0°$ is the direction to the analyzer axis), and the photoelectron distribution (I) is recorded as functions of θ, α, and E_B, where θ is the rotation angle of $\boldsymbol{e}_z$ with respect to the analyzer axis and E_B is the binding energy referenced to E_F of gold. The spectra are recorded at 10 K with an energy resolution of ~3 meV.

In general, a photoemission event from a given initial-to-final state ($|\Psi_i\rangle$ to $|\Psi_f\rangle$) under a given experimental setup has the same cross section to another event which is a mirror reflection of the original one [14]. Here, everything should be reflected, not just the crystal and the incident light, but also $|\Psi_{i,f}\rangle$ into $|\tilde{\Psi}_{i,f}\rangle \equiv \hat{\Pi}|\Psi_{i,f}\rangle$, and even the direction of the circulating currents responsible for magnetism, if any. We consider a one-step photoemission process, so that $|\Psi_f\rangle$ is an inverse low-energy electron diffraction (LEED) state extending from the sample into

the detector [5] and evaluate the operator under a dipole approximation: $I^{\pm} \propto |\langle \Psi_f | \boldsymbol{A}^{\pm}_{\rm pes} \cdot \hat{\boldsymbol{p}} | \Psi_i \rangle|^2$.

When the incidence plane matches the mirror plane of the crystal, the result $\tilde{I}^{+}$ obtained in a reflected experiment with respect to the incidence plane (this coincides with the apparatus' mirror plane in our experimental geometry) is the same as that of the original experiment with a reversed circular polarization I^{-}, as can be seen by comparing Figs. 1(b1) and 1(b2). One can confirm $|\langle \Psi_f | \boldsymbol{A}^{+}_{\rm pes} \cdot \hat{\boldsymbol{p}} | \Psi_i \rangle| = |\langle \tilde{\Psi}^{x}_{f} | \boldsymbol{A}^{-}_{\rm pes} \cdot \hat{\boldsymbol{p}} | \tilde{\Psi}^{x}_{i} \rangle|$ [the left- and right-hand sides of this equation correspond to the events shown in Figs. 1(b1) and 1(b2), respectively] with the aid of $\hat{\Pi}_x (\boldsymbol{A}^{+}_{\rm pes} \cdot \hat{\boldsymbol{p}}) \hat{\Pi}_x = \boldsymbol{A}^{+}_{\rm pes} \cdot (-\hat{p}_x \boldsymbol{e}_x + \hat{p}_y \boldsymbol{e}_y + \hat{p}_z \boldsymbol{e}_z) = \frac{A}{2}(1, -i\cos\eta, -i\sin\eta) \cdot \hat{\boldsymbol{p}} = -\boldsymbol{A}^{-}_{\rm pes} \cdot \hat{\boldsymbol{p}}$. Therefore $I^{+}(\theta, \alpha, E_B) = I^{-}(\theta, -\alpha, E_B)$, so that the angular distribution of the dichroism $I^{D} = I^{+} - I^{-}$ acquires a vertical node, i.e., $I^{D}(\theta, 0°, E_B) = 0$.

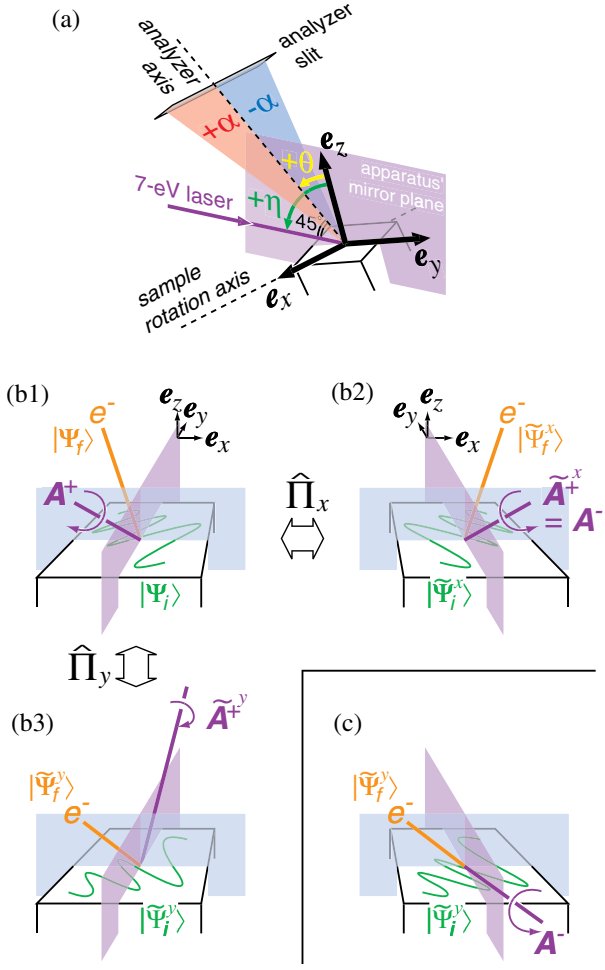

FIG. 1 (color online). A bird's-eye view of photoemission. (a) ARPES geometry. The polarization of the laser is controlled by a wave plate [13]. (b1) Photoemission by a right circularly polarized photon. (b2) and (b3) are mirror reflections of (b1) with respect to the $x = 0$ (incidence) plane and $y = 0$ plane, respectively. $\hat{\Pi}_l$ ($l = x$ or y) is the operator for the reflection with respect to the $l = 0$ plane. A tilde accompanied by l is attached to the reflected states and the reflected vector potentials. (c) A configuration for achieving photoemission into $|\tilde{\Psi}^{y}_{i}\rangle$. Note the resemblance of (c) and (b3) up to the direction of the rotation of the vector potentials in the xy plane.

Next, we consider a case where the mirror plane of the crystal is vertical to the incidence plane and ask whether

$$I^{+}(\theta, \alpha, E_B) = I^{-}(-\theta, \alpha, E_B) \tag{1}$$

can hold. This corresponds to investigating whether the matrix elements for the events shown in Figs. 1(b1) and 1(c) can be equivalent or not. The incidence angles are different, since the laser and the analyzer are fixed in space; thus, these two photoemission events cannot overlap by any symmetry operations. Therefore, Eq. (1) does not hold globally. Nevertheless, the events shown in Figs. 1(b3) and 1(c) [the former is a reflection of Fig. 1(b1) with respect to the zx mirror plane, and hence, equivalent to the event of Fig. 1(b1)] resemble each other: In both cases, the initial and final states are the same, and the in-plane (xy) components of $\boldsymbol{A}$ rotate anticlockwise on the sample surface. Explicitly, Eq. (1) is equivalent to

$$\left| \langle \tilde{\Psi}^{y}_{f} | \begin{pmatrix} -1 \\ i\cos\eta \\ -i\sin\eta \end{pmatrix} \cdot \hat{\boldsymbol{p}} | \tilde{\Psi}^{y}_{i} \rangle \right| = \left| \langle \tilde{\Psi}^{y}_{f} | \begin{pmatrix} -1 \\ i\cos(\eta + 2\theta) \\ i\sin(\eta + 2\theta) \end{pmatrix} \cdot \hat{\boldsymbol{p}} | \tilde{\Psi}^{y}_{i} \rangle \right|, \tag{2}$$

and the main difference occurs in the sign (phase) of the z component of the vector potential with respect to the x and y components. Thus, when

$$|\langle \Psi_f | \hat{p}_z | \Psi_i \rangle| \ll |\langle \Psi_f | \hat{p}_{x,y} | \Psi_i \rangle| \tag{3}$$

is fulfilled, Eq. (2) and, hence, Eq. (1) hold at $\theta \sim 0°$, resulting in a horizontal node $I^{D}(0°, \alpha, E_B) = 0$.

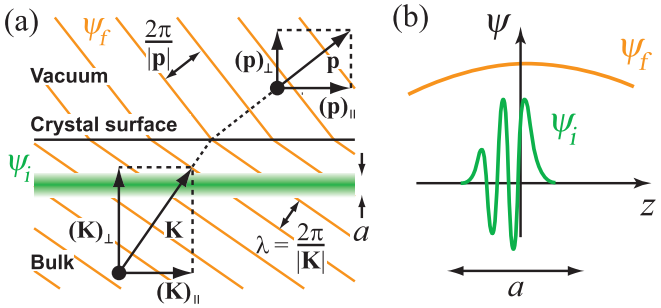

FIG. 2 (color online). Photoemission from a 2D state into an inverse LEED state. (a) The 2D and inverse LEED states. Orange lines show wave fronts that are refracted at the surface. (b) The wave functions of the 2D and inverse LEED states.

The condition (3) is fulfilled when Ψ_i is two-dimensional (2D) and spatially confined in the z direction within a length scale a shorter than the de Broglie wavelength λ of the photoelectron final state, as shown in Fig. 2. Then, $\int_{-\infty}^{\infty} dz \Psi_f^*(x,y,z) \frac{\hbar}{i} \frac{\partial}{\partial z} \Psi_i(x,y,z) \sim \Psi_f^*(x,y,0) \int_{-a}^{a} dz \frac{\hbar}{i} \frac{\partial}{\partial z} \Psi_i(x,y,z) = 0$, so that the photoemission matrix element becomes susceptible only to the in-plane component of the vector potential. The small photoelectron kinetic energy E_{kin} achieved by the 7-eV laser is favorable for satisfying condition (3), since $\lambda[\text{Å}] \sim 12/\sqrt{E_{\mathrm{kin}}[\mathrm{eV}]}$. Even when λ becomes comparable to a, $\Psi_i(z)$ is usually an oscillating function for $|z| \lesssim a$, and, therefore, the matrix element has little dependence on the $\hat{p}_z$ component.

The case for $SrTiO_3$:Nb.—$SrTiO_3$ is an oxide semiconductor having a cubic perovskite structure. The bulk can be doped with carriers by incorporating Nb. Recently, it has been revealed that an inversion layer occurs at the surface of semiconducting $SrTiO_3$ independent of the carrier concentration of the bulk [15,16].

We find that the 2D electron gas formed in the inversion layer of $SrTiO_3$ is an ideal case that exhibits the horizontal and vertical nodes. In Fig. 3, we show the angular distribution of the spectral weight near E_F recorded on a (001) surface of 1%-Nb-doped $SrTiO_3$ annealed in vacuum for 40 min at 550 °C. Here, [100] and [010] are aligned to $\boldsymbol{e}_x$ and $\boldsymbol{e}_y$, respectively, within 5°. A circular Fermi surface can be observed in the $I^+ + I^-$ mapping (a), and I^+ (b) appears to be a reflection of I^- (c) about both the θ and α axes. Therefore, horizontal and vertical nodes occur in I^D (d). The vertical node can be understood as a result of the (100) mirror plane matching the incidence plane, and the horizontal node can be understood from the facts that the (010) mirror plane is vertical to the incidence plane and the electronic state is 2D. The normalized dichroic asymmetry $I^D/(I^+ + I^-)$ is a maximum (>60%) around $\theta = \pm\alpha$. The spectral weight mapped by s (p) polarization is bright (dark) at $\alpha = 0°$ and dark (bright) at $\theta = 0°$ [see Figs. 3(e) and 3(f)], indicating that the states probed by the 7-eV laser consist of d_{xy} orbitals having odd parity with respect to the reflection at the $x = 0$ and $y = 0$ planes [15–17]. The in-plane orbital character of the initial states may further facilitate the condition of the 2D confinement to be fulfilled.

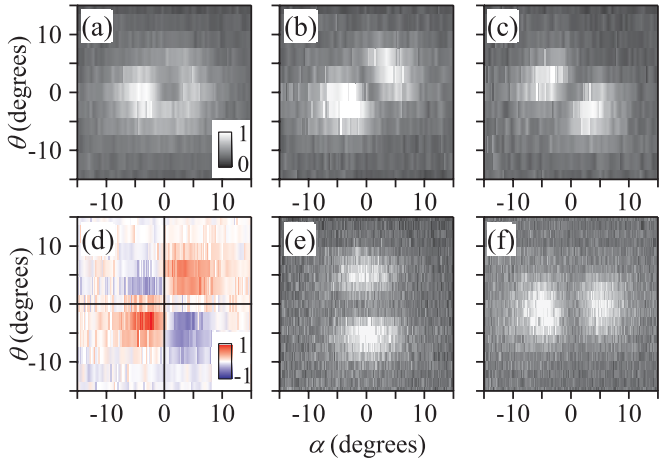

FIG. 3 (color online). Spectral intensity distributions ($|E_B| \leq 5$ meV) of $SrTiO_3$:Nb recorded by various polarizations. (a) $(I^+ + I^-)/2$. (b) I^+. (c) I^-. (d) I^D showing a sign change around $\alpha = 0°$ (vertical node) and $\theta = 0°$ (horizontal node). (e) I^s. (f) I^p.

The case for $Cu_xBi_2Se_3$.—Bi_2Se_3 is found to be a topological insulator [18,19] supporting a single Dirac-cone dispersion on its surface [20–22]. Cu intercalation effectively dopes the system with electron carriers [23,24]. In the present case, the nominal Cu concentration is $x = 0.17$, and E_F is located 480 meV above E_D, as shown in Fig. 4(a). The band dispersion in the k_xk_y plane (k_x is set along $\bar{\Gamma}$-$\bar{M}$ and is parallel to $\boldsymbol{e}_x$ within 3°) changes from nearly isotropic to hexagonal in going away from E_D. This can be explained within a 2D $k \cdot p$ Hamiltonian constrained under C_{3v} and time-reversal symmetry [25,26]:

$$H(k) = v_k(k_x\sigma_y - k_y\sigma_x) + k^2/2m^* + \xi/2(k_+^3 + k_-^3)\sigma_z. \quad (4)$$

Here, ξ is responsible for the hexagonal warping, σ_i is the Pauli matrix, $k_\pm = k_x \pm ik_y$, v_k contains a k^2-order correction, and $1/m^*$ introduces particle-hole asymmetry. The threefold pattern observed in the mappings at $E_B \geq 0.54$ eV originates from the bulk valence band, and the faint intensity observed inside the hexagon near E_F is due to the bulk conduction band [24].

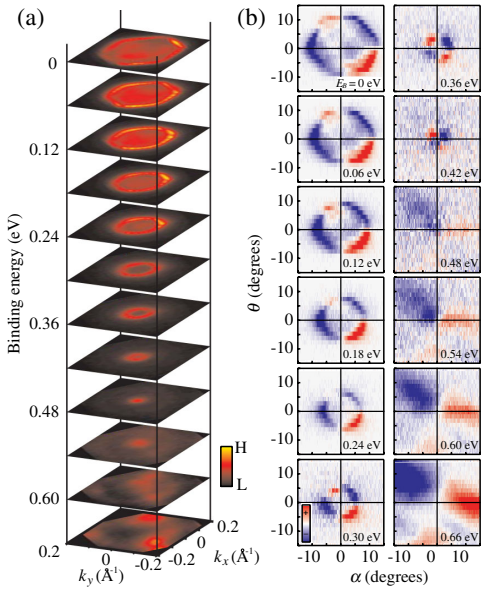

FIG. 4 (color online). CDAD of Cu-doped Bi_2Se_3. (a) Electronic structure recorded by ARPES on the (111) surface of $Cu_xBi_2Se_3$. Here, $I^+ + I^-$ is converted into k-space map. The single crystal is grown from the melt. (b) I^D at various E_B's. Also refer to Ref. [32].

In Fig. 4(b), we show I^D at various E_B's. In the vicinity of E_D (at $E_B = 0.42$ and 0.36 eV), we observe nodal lines at $\theta = 0°$ and $\alpha = 0°$. This can be explained by noting that the effective Hamiltonian [Eq. (4)] up to second order in k is invariant under mirror operations at the $x = 0$ and $y = 0$ planes, and the states therein are 2D, so that the conditions for the horizontal and the vertical nodes are fulfilled. Note that it is the effective Hamiltonian, not the crystal surface, that has the mirror symmetry about the $x = 0$ plane. On the other hand, I^D in the bulk valence-band region at $E_B \geq 0.54$ eV does not show the vertical node since the crystal does not have a vertical mirror plane. It also does not show the horizontal node since the valence-band electronic structure is three-dimensional, even though the crystal has a horizontal mirror plane at $y = 0$.

It is apparent that the horizontal node in the topological state is gradually distorted in going from E_D to E_F, even though the crystal as well as the effective Hamiltonian has horizontal mirror symmetry. This indicates that the topological states lose the condition of 2D confinement at large k, and around E_F, they penetrate deep into the bulk rather than being surface states localized on surface layers. This is supported by calculations [27] and is reminiscent of a surface-state-to-surface-resonance transition with varying k observed in the states on metal surface [28]. The results thus indicate that the effective Hamiltonian Eq. (4) is valid only in the vicinity of E_D. The deviation from Eq. (4) may be important to understand the possibly exotic superconductivity of $Cu_xBi_2Se_3$ [23,24,29,30] and the recent observation of the topological states away from E_D acquiring out-of-plane spin components [31].

In summary, we find that the CDADs of both $SrTiO_3$:Nb around E_F and Cu-doped Bi_2Se_3 around E_D exhibit a flower-shaped pattern having horizontal and vertical nodes. The vertical node is explained within a well-known geometric effect [5], whereas the horizontal node can be understood by using a combination of the geometry and the 2D character of the initial electronic state. The length scale of the 2D confinement of the initial state is set by the de Broglie wavelength of the photoelectron final state. The horizontal node in CDADs can therefore be a measure of the two-dimensionality of the electronic states, providing information of the penetration depth of surface states and insights into the 2D electron gas formed on semiconductor surfaces.

This research is supported by JSPS through its FIRST Program. H. Y. H. and C. B. acknowledge support by the Department of Energy, Office of Basic Energy Sciences, Division of Materials Sciences and Engineering, under Contract No. DE-AC02-76SF00515.

*Present address: Universität Würzburg, Experimentelle Physik VII and Röntgen Research Center for Complex Materials RCCM, Am Hubland, D-97074 Würzburg, Germany.

[1] B. T. Thole, P. Carra, F. Sette, and G. van der Laan, Phys. Rev. Lett. **68**, 1943 (1992).
[2] P. Carra, B. T. Thole, M. Altarelli, and X. Wang, Phys. Rev. Lett. **70**, 694 (1993).
[3] W. Kuch and C. M. Schneider, Rep. Prog. Phys. **64**, 147 (2001).
[4] R. L. Dubs, S. N. Dixit, and V. McKoy, Phys. Rev. Lett. **54**, 1249 (1985).
[5] G. Schonhense, Phys. Scr. **T31**, 255 (1990).
[6] T. Matsushita *et al.*, Phys. Rev. B **56**, 7687 (1997).
[7] A. Kaminski *et al.*, Nature (London) **416**, 610 (2002).
[8] S. V. Borisenko *et al.*, Phys. Rev. Lett. **92**, 207001 (2004).
[9] M. Mulazzi *et al.*, Phys. Rev. B **74**, 035118 (2006).
[10] F. Vidal *et al.*, Phys. Rev. B **76**, 081302(R) (2007).
[11] V. B. Zabolotnyy *et al.*, Phys. Rev. B **76**, 024502 (2007).
[12] D. V. Vyalikh *et al.*, Phys. Rev. Lett. **100**, 056402 (2008).
[13] T. Kiss *et al.*, Rev. Sci. Instrum. **79**, 023106 (2008).
[14] D. Venus, Phys. Rev. B **48**, 6144 (1993).
[15] A. F. Santander-Syro *et al.*, Nature (London) **469**, 189 (2011).
[16] W. Meevasana *et al.*, Nature Mater. **10**, 114 (2011).
[17] A. Damascelli, Z. Hussain, and Z.-X. Shen, Rev. Mod. Phys. **75**, 473 (2003).
[18] L. Fu, C. L. Kane, and E. J. Mele, Phys. Rev. Lett. **98**, 106803 (2007).
[19] M. Z. Hasan and C. L. Kane, Rev. Mod. Phys. **82**, 3045 (2010).
[20] H.-J. Zhang, C.-X. Liu, X.-L. Qi, X. Dai, Z. Fang, and S.-C. Zhang, Nature Phys. **5**, 438 (2009).
[21] Y. Xia *et al.*, Nature Phys. **5**, 398 (2009).
[22] D. Hsieh *et al.*, Nature (London) **460**, 1101 (2009).
[23] Y. S. Hor *et al.*, Phys. Rev. Lett. **104**, 057001 (2010).
[24] L. A. Wray *et al.*, Nature Phys. **6**, 855 (2010).
[25] L. Fu, Phys. Rev. Lett. **103**, 266801 (2009).
[26] K. Kuroda *et al.*, Phys. Rev. Lett. **105**, 076802 (2010).
[27] W. Zhang, R. Yu, H.-J. Zhang, X. Dai, and Z. Fang, New J. Phys. **12**, 065013 (2010).
[28] P. O. Gartland and B. J. Slagsvold, Solid State Commun. **25**, 489 (1978).
[29] M. Kriener, K. Segawa, Z. Ren, S. Sasaki, and Y. Ando, Phys. Rev. Lett. **106**, 127004 (2011).
[30] L. Fu and E. Berg, Phys. Rev. Lett. **105**, 097001 (2010).
[31] S. Souma *et al.*, Phys. Rev. Lett. **106**, 216803 (2011).
[32] See Supplemental Material at http://link.aps.org/supplemental/10.1103/PhysRevLett.107.077601 for a movie file showing how the CDAD pattern evolves with energy.